

Synergistic mechanisms for the superior sorptive removal of aquatic pollutants via functionalized biochar-clay composite

Maged Ali, Elgarahy Ahmed M., Hlawitschka Mark W., Haneklaus Nils H., Gupta Ashok Kumar, Bhatnagar Amit

This is a Publisher's version
published by Elsevier
in Bioresource Technology

version of a publication

DOI: 10.1016/j.biortech.2023.129593

Copyright of the original publication:

© The Author(s)

Please cite the publication as follows:

Maged, A., Elgarahy, A. M., Hlawitschka, M. W., Haneklaus, N. H., Gupta, A. K., Bhatnagar, A. (2023). Synergistic mechanisms for the superior sorptive removal of aquatic pollutants via functionalized biochar-clay composite. Bioresource technology. DOI: 10.1016/j.biortech.2023.129593

**This is a parallel published version of an original publication.
This version can differ from the original published article.**



Synergistic mechanisms for the superior sorptive removal of aquatic pollutants via functionalized biochar-clay composite

Ali Maged^{a,b,*}, Ahmed M. Elgarahy^{c,d,*}, Mark W. Hlawitschka^e, Nils H. Haneklaus^f, Ashok Kumar Gupta^g, Amit Bhatnagar^a

^a Department of Separation Science, LUT School of Engineering Science, LUT University, Sammonkatu 12, FI-50130 Mikkeli, Finland

^b Geology Department, Faculty of Science, Suez University, P.O. Box 43518, El Salam City, Suez Governorate, Egypt

^c Environmental Chemistry Division, Environmental Science Department, Faculty of Science, Port Said University, Port Said, Egypt

^d Egyptian Propylene and Polypropylene Company (EPPC), Port Said, Egypt

^e Institute of Process Engineering, Johannes Kepler University Linz, Altenberger Straße 69, 4040 Linz, Austria

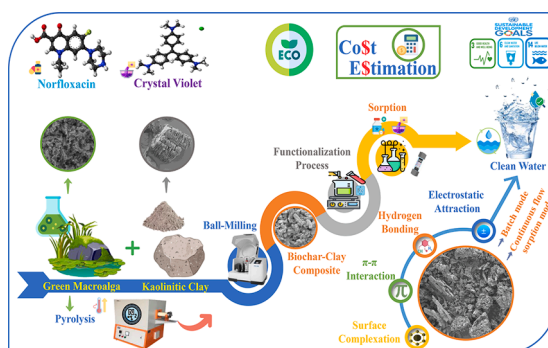
^f Td Lab Sustainable Mineral Resources, University for Continuing Education Krems, Dr. Karl-Dorrek-Straße 30, 3500 Krems, Austria

^g Environmental Engineering Division, Department of Civil Engineering, Indian Institute of Technology Kharagpur, Kharagpur 721302, India

HIGHLIGHTS

- The functionalized biochar-clay composite (FBKC) was successfully synthesized.
- FBKC exhibited specific surface area of 221.04 m²/g compared to 47.02 m²/g for BC.
- Synergistic sorption mechanisms were confirmed for NFX and CVD sorption by FBKC.
- FBKC showed a maximum column bed capacity of 37.90 (NFX) and 53.98 mg/g (CVD).
- The cost estimation of FBKC was precisely presented, indicating a rate of 5.72 €/kg.

GRAPHICAL ABSTRACT



ARTICLE INFO

Keywords:

Biochar
Norfloxacin
Crystal violet
Adsorption mechanism
Cost estimation

ABSTRACT

This study investigated the successful synthesis of functionalized algal biochar-clay composite (FBKC). Subsequently, the sorption performance of FBKC towards norfloxacin (NFX) antibiotic and crystal violet dye (CVD) from water was extensively assessed in both batch and continuous flow systems. A series of characterization techniques were carried out for FBKC and the utilized precursors, indicating that the surface area of FBKC was increased thirty-fold with a well-developed pore structure compared to the original precursors. FBKC demonstrated a maximum sorption capacity of 192.80 and 281.24 mg/g for NFX and CVD, respectively. The suited fitting of the experimental data to Freundlich and Clark models suggested multi-layer sorption of NFX/CVD molecules. The mechanistic studies of NFX/CVD sorption onto FBKC unveiled multiple mechanisms, including π - π interaction, hydrogen bonding, electrostatic attraction, and surface/pore filling effect. The estimated cost of 5.72 €/kg and superior sorption capacity makes FBKC an efficient low-cost sorbent for emergent water pollutants.

* Corresponding authors.

E-mail addresses: Ali.Maged@suezuni.edu.eg, Ali.Gharieb@lut.fi (A. Maged), ahmed.gamal@sci.psu.edu.eg (A.M. Elgarahy).

<https://doi.org/10.1016/j.biortech.2023.129593>

Received 12 June 2023; Received in revised form 28 July 2023; Accepted 30 July 2023

Available online 7 August 2023

0960-8524/© 2023 The Author(s). Published by Elsevier Ltd. This is an open access article under the CC BY license (<http://creativecommons.org/licenses/by/4.0/>).

1. Introduction

Emergent pollutants have become a growing concern in recent years owing to their detrimental potential to the ecosystem and human health. Emerging and legacy pollutants such as dyes, microplastics, poly-fluoroalkyl substances, and pharmaceuticals have been detected in water sources worldwide, including potable water sources (Aneesh et al., 2023). Effective management of emergent pollutants in water requires a multifaceted approach that includes monitoring, effective treatment, and regulatory measures to limit their release into the environment. Pharmaceutical compounds and dyes are the most concerning aspects of water pollution due to their ability to persist in the aquatic environment and accumulate in living organisms.

Cationic dyes are commonly utilized in various industrial applications, surpassing other dye categories (Pandey et al., 2023). Moreover, cationic dyes exhibit a non-biodegradable/non-photodegradable behavior and possess a hazardous nature. Crystal violet dye (CVD), classified as a cationic dye, is frequently detected in industrial wastewater owing to its extensive usage as a coloring agent in textile, detergent, cosmetics, printing, and fertilizer industries (see [supplementary material](#)). The presence of CVD in water significantly affects humans and aquatic organisms due to their highly mutagenic, clastogenic, genotoxic, and carcinogenic nature (Uddin et al., 2023). Antibiotics represent a prominent class of emerging contaminants, extensively detected in the aquatic environment due to their widespread application as the third most commonly prescribed pharmaceuticals (> 6% of total prescription drugs) (Ohale et al., 2023). Norfloxacin (NFX), one of the fluoroquinolones classes, is a synthetic broad-spectrum antibiotic commonly prescribed for treating urinary tract infections and Gram (+/-) bacteria as well as veterinary medicine (see [supplementary material](#)). The detected NFX concentrations in the surface water and wastewater were reported to be up to 1150 ng/L and 0.75 µg/L, respectively (Ohale et al., 2023). Although low concentrations of antibiotic residues may not directly harm humans, prolonged consumption of contaminated water can lead to adverse health effects, including muscle and liver damage, nausea, vomiting, and diarrhea (Abd El-Fattah et al., 2023). Therefore, eliminating these emerging contaminant residues from the effluents before their release into the environment is instantly paramount. Consequently, selecting appropriate sorbents that possess substantial surface area, active surface functional groups, and well-developed porous structure, in addition to reasonable cost and availability of precursors such as biochar and clays, are considered significant.

Biochar derived from marine algae (macro), third-generation feedstocks for biofuel production, has gained significant attention due to their abundance, effortless harvesting, and substantial production rate (Nguyen et al., 2022). Algal biochar and its various modified forms showed a superior performance towards eliminating emerging contaminants from aqueous solutions. However, comparing the adsorptive performance of biochar to activated carbon showed limited potential towards the existing pollutants in water due to their layer structure (single carbon layer) and relatively low surface area and pore size. Therefore, impregnating biochar with specific layered-structure materials such as clay minerals as composite could enhance the ability to adsorb ionizable adsorbates. Kaolinitic clay is a well-known aluminosilicate clay rich in kaolinite minerals with a 1:1 type layer structure (aluminum: silicon) (Maged et al., 2023b). The potentiality of using clays in removing various contaminants has been successfully proven in the literature owing to the negatively charged layers, interlayer exchangeable cations (i.e., Mg^{2+} , Na^{+} , Ca^{2+}), porosity, and specific surface area. Moreover, biochar within the biochar-clay composites can provide an appropriate surface for the kaolinite particles distribution. Consequently, biochar's sorptive performance can be enhanced by employing structural modifications (such as co-precipitation and ball-milling techniques) and impregnation with clay materials. Ball-milling (involving the mechanical grinding of the clay and biochar precursors together) enhances interfacial contact between clay and biochar,

promoting synergistic effects and improving the overall performance of the composite material. The co-precipitation method offers advantages such as precise control over the composition, morphology, functionalization, and particle size distribution of the obtained composite (Foong et al., 2022). Combining these techniques to prepare clay-biochar composites allows the development of tailored composite materials with desirable properties for eliminating a wide range of emerging contaminants from an aqueous solution.

The overarching aim of this study was to develop a straightforward method for synthesizing a low-cost engineered functionalized biochar-clay composite (FBKC) utilizing algal biomass and natural kaolinitic clay. The engineered composite was successfully synthesized through three simple steps of pyrolysis, ball milling, and co-precipitation methods to achieve the highest sorptive performance towards the targeted pollutants. The applied methods aimed to improve the performance of FBKC composite to be a multifunctional sorbent able to eliminate various pollutants through varied sorption mechanisms. Various analytical techniques extensively characterized the prepared FBKC and the initial precursors (BC and KC). The FBKC sorbent was subsequently employed for NFX/CVD sorption via two aqueous sorption systems (batch and dynamic (fixed-bed column) modes). Furthermore, the confirmed governing sorption mechanisms of NFX/CVD onto FBKC were successfully investigated and discussed. Finally, a concise presentation of the cost estimation of FBKC was provided.

2. Materials and methods

2.1. Feed stocks and reagents

Marine green alga *Enteromorpha flexuosa* (harvested from El-Gameil coast, Mediterranean Sea, Egypt) was used as a feedstock in the biochar synthesis. The green alga was thoroughly underwent a rigorous cleansing process (*in situ*) consisting of three successive washes with normal water to eradicate any accumulated dirt effectively. Thereafter, the algal mass was transferred to the laboratory for the necessary pretreatment in an airtight-plastic bottle (labeled as MGA) to prevent any moisture intrusion. The pulverization of the alga into powder form was accomplished with the aid of a pestle and mortar. The resulting algal biomass was subsequently sieved and stored within an airtight plastic bottle until further usage. Natural Kaolinitic clay samples were obtained from Abu Zenima area, South Sinai, Egypt. The utilized KC samples were specifically collected (lumped form) from the Kaolinitic-bearing members of the Matulla Formation, which outcropped at Abu Zenima area. Thereafter, the KC samples were subjected to a pretreatment process, as reported previously by Maged et al. (2023a). Thereafter, the samples were stored and labeled as KC.

2.2. Synthesis of functionalized biochar-clay composite

The dried MGA powder was subjected to a rigorous pyrolysis process (tube furnace, 600 °C, 3.0 h) with a rate of 5 °C/min and a nitrogen flow of 0.1 L/min (continuous flow). The determined biochar yield after the pyrolysis process was found to be 39%. The sample subsequently underwent a further washing procedure utilizing deionized water to ensure the complete removal of any residual impurities from the obtained material. The resulting biochar (BC) was dried (105 °C, 6 h). The precursor materials, KC and BC, with a specific mass ratio (1:1 wt%), were carefully placed within a specialized ball-milling container at a precise mass ratio of 1:100. The ball mill was subsequently automated to operate at 600 rpm for 5 h and labeled as KC-BC.

For the functionalized biochar-clay composite, the co-precipitation method was applied for the KC-BC composite. Briefly, 25 g of KC-BC composite was mixed with a 2:1 M ratio of $FeCl_3 \cdot 6H_2O$ (M^{3+}) and $FeSO_4 \cdot 7H_2O$ (M^{2+}) in a 250 mL round-bottomed flask with continuous stirring for 90 min. Subsequently, the suspension was heated at 80 °C while being magnetically stirred for a further 45 min. Afterward, 40 mL

of the precipitating agent (1.0 M NaOH) was gradually added under constant stirring at 80 °C. The formation of a black precipitate indicated the successful synthesis of the functionalized KC-BC composite. Finally, the resultant functionalized composite was separated from the synthesis medium using a neodymium magnet, washed twice, dried (90 °C, 24 h), and labeled as FBKC. The final sorbent form (FBKC) and the utilized precursors were characterized, and their adsorption properties were subsequently investigated. Thereafter, the stability test of FBKC was performed (see [supplementary material](#)). Furthermore, a screening test was performed, and the results showed that the composite and FBKC have a higher sorption capacity compared to the original precursors (BC and KC) (see [supplementary material](#)).

2.3. Batch and column (fixed-bed) studies

The equilibrium batch experiments were conducted in capped 100 mL glass bottles containing a sorbent amount of 0.4 g/L, a measured volume of NFX and CVD solution, and a known concentration of NFX and CVD. The bottles (containing NFX/CVD and FBKC) were agitated (200 rpm) in an orbital shaker for a known period (up to 300 min) at room temperature. Freshly prepared solutions (0.1 M NaOH/HCl) were employed to adjust the pH of the solutions. The impact of several experimental conditions on the sorption of NFX/CVD onto FBKC was also investigated to optimize the batch sorption process. The influence of solution pH (2–9), adsorbent quantity (0.1–1.0 g/L), adsorbent-adsorbate interaction time (0–300 min), initial NFX/CVD concentration (5–200 mg/L), and ionic strength (NaCl, 0.02 – 0.10 M) were investigated in triplicate through the adsorption process to ensure reproducibility and standard deviations were calculated (maximum 2% error; shown via error bars). The suspension, after equilibration, was filtered, and the residual concentration of NFX and CVD was determined via UV–vis spectrophotometer at λ_{max} of 278 and 584 nm, respectively. Furthermore, FBKC was evaluated in a continuous-flow system to validate its capability for scaling up the process. The column preparation, parameters, applied equations, models, and calculations were conducted according to [Maged et al. \(2023c\)](#). All column experimental runs were performed in duplicate (mean values and standard deviations are presented via error bars) under the same conditions for each run.

3. Results and discussion

3.1. Characterization studies

3.1.1. XRD analysis

The XRD mineral phases of the algal BC exhibited amorphous characteristics with the detection of XRD reflection around $2\theta = 26.00^\circ$ and 44.00° , corresponding to the diffraction planes 111 and 002, respectively ([Qin et al., 2023](#)). The detection of these peaks for BC indicates the presence of amorphous carbon of the successfully obtained algal BC. Moreover, the obtained XRD results of KC evidenced that well-crystallized (001) kaolinite ($2\theta \approx 12.20^\circ$) and quartz ($2\theta \approx 26.83^\circ$) are the dominant constituents of utilized clay ([Maged et al., 2023a](#)). For the engineered functionalized composite, the XRD spectra of FBKC showed the characteristic reflections of the involved precursors (BC, KC, and magnetite) crystal planes (see [supplementary material](#)). However, in some cases, the detected peaks exhibited a reduced intensity and disappearance of the existing phases, implying that the composite structure became more amorphous. The XRD pattern of the magnetite-loaded composite (FBKC) demonstrated seven sharp characteristic peaks of magnetite at 2θ values of 32.66° , 35.65° , 38.13° , 43.39° , 53.66° , 58.01° , and 61.91° , corresponding to the (220), (311), (222), (400), (422), (511), and (440) of the magnetite (JCPDS card no. 11–0614) and hematite (JCPDS card no. 33–0664) crystal planes, respectively. The peaks of FBKC at $2\theta = 12.29^\circ$, 26.93° , and 38.85° correspond to the primary KC crystal structure, evidencing that KC particles were successfully impregnated onto the BC surface.

Furthermore, a new peak was detected at $2\theta \approx 8.76^\circ$ for the kaolinite mineral, which possesses an increased interlayer spacing (d_{001}) of KC (10.17 \AA) as compared to the 7.26 \AA value of raw KC. This phenomenon could be ascribed due to the insertion of BC and iron particles into the interlayer space ([Maged et al., 2023c](#)). This hypothesis is reinforced by the findings from the FT-IR analysis ([Section 3.1.2.](#)) and explains the superior sorption capacity of FBKC compared to original precursors.

3.1.2. FT-IR analysis

The transmittance spectra for BC, KC, and FBKC showed substantial variations between utilized precursors and FBKC composite (see [supplementary material](#)). Precisely, the FT-IR spectrum of the obtained FBKC composite reflects the enriched functional groups on the FBKC sorbent surface, which consequently explains the significant sorption performance of the composite. The band around 1430 cm^{-1} is assigned to C = O of the carboxyl group. The sharp band in the $1500\text{--}1700 \text{ cm}^{-1}$ range is attributed to the C = C and C = O vibrations, which could be ascribed to BC's aromatic ring stretching. However, the vibration of the methyl group was observed by the band around $2850\text{--}3000 \text{ cm}^{-1}$. Hydroxyl group stretching at 3655 cm^{-1} and Si–O stretching at 1050 cm^{-1} were the characteristics of KC spectra. Nonetheless, the observed broadening after the preparation of FBKC implies the intercalation of specific groups within the layers of the KC, resulting in a slight displacement towards the higher wavenumber region. Additionally, the Si–O and Al–OH deformation bands in the KC spectrum appeared in the range of $1015\text{--}912 \text{ cm}^{-1}$ in which these bands were stretching at 1015 cm^{-1} and bending at 913 cm^{-1} , respectively. The functionalized composite FBKC showed a new appearance of bands in the same wavelength ranges compared to utilized biochar and clay. These findings indicate that the iron functionalization of FBKC significantly increased the surface functional groups. Furthermore, The characteristic bands of FBKC around $500\text{--}600 \text{ cm}^{-1}$ are ascribed to the Fe–O stretching vibrations (see [supplementary material](#)), which were accredited to the formation of Fe_xO_y nanoparticles ([Wang et al., 2019](#)). Consequently, incorporating Fe–O as active groups onto the FBKC surface is anticipated to the observed increase in the sorption potential for the targeted pollutants. The aforementioned observations support the successful synthesis of FBKC composites based on BC and KC.

3.1.3. Raman analysis

The variation in the Raman spectra between BC and FBKC is presented (see [supplementary material](#)). The D band corresponded to the sp^3 vibrational mode of amorphous carbon and was detected around a wavelength of 1300 cm^{-1} , indicating the presence of lattice imperfections in the carbon structure. However, the band observed around 1550 cm^{-1} corresponds to the G band, which is a distinctive absorption feature resulting from the in-plane sp^2 hybridized C–C bond stretching vibration. This peak signifies the presence of a well-maintained graphitic structure. The I_D/I_G ratio (intensities ratio) is a significant parameter for evaluating the degree of graphitization in carbon-based materials. The good I_D/I_G ratio (0.84) of BC suggests that BC comprises a substantial amount of both ordered and disordered graphitic carbon structures (see [supplementary material](#)). However, the I_D/I_G ratio of FBKC (1.08) was higher than BC, indicating that Fe modification enhances the graphitization degree ([Al-Lagtah et al., 2016](#)). Furthermore, the closer the resemblance between the structural characteristics of BC and FBKC and graphite, the more conducive to creating robust $\pi\text{--}\pi$ conjugated structures with benzene rings and similar structures, which enhances the sorption favorability for organic pollutants such as CVD and NFX. The G' band (2D-band) arises from a two-phonon lattice vibration process and is considered the second-order overtone of the D-band. Typically, the G' band is employed for evaluating the thickness of graphene layers. In single-layer graphene, this band exhibits a sharper and more pronounced peak compared to multi-layer graphene (see [supplementary material](#)). The 2D band is commonly utilized to ascertain the thickness of graphene layers. It exhibits greater sharpness and intensity in single-

layer graphene compared to multi-layer graphene. Based on the obtained Raman results, the FBKC structure entails a graphitic structure consisting of multiple graphene layers (Sajjadi et al., 2021).

3.1.4. Elemental composition

Fig. 1 illustrates the elemental composition (wt.%) of BC, KC, and FBKC. The percentages of O, Al, Na, and Si elements for FBKC were higher than BC, which mainly attributed to introduction of KC element contents (Fig. 1). Various ions, such as Fe, K, Na, and Cu, were initially observed in the KC sample. The presence of these cations in the KC specimens is referred to as polycationic KC, which is advantageous for the sorption process (Maged et al., 2020). Moreover, the magnetic modification of the synthesized composite significantly increased the O content of FBKC, consequently increasing the O-containing functional groups. This could potentially promote the formation of hydrogen bonds with targeted pollutant molecules, subsequently augmenting the sorption capacity. Additionally, the EDS analysis revealed that the Fe content was dramatically increased in FBKC due to iron modification (Fig. 1). These findings confirmed that iron was successfully impregnated to BC and KC composite by increasing Fe percentage and the presence of corresponding peaks.

3.1.5. Surface morphology and measurements

The surface morphology (via SEM images) of the utilized FBKC sorbent (biochar-clay composite) and its original precursors BC and KC are depicted in Fig. 1, respectively. A highly porous surface was observed on the biochar surface (Fig. 1). However, the SEM micrograph of KC exhibited irregular-hexagonal layered-structure (flaky-structure) formations (Fig. 1). The SEM analysis of FBKC (Fig. 1) showed that BC particles adhered to the clay surfaces, resulting in a more uneven morphology on the clay and biochar surfaces, which, in turn, furnished a greater reactive surface area for sorption than the standalone biochar. However, the clay particles did not entirely encapsulate the biochar surface and vice versa, thus maintaining the accessibility of the biochar pores and clay layer to adsorbate molecules. Furthermore, Fig. 1 illustrates that a considerable number of Fe-nanoparticles were impregnated onto the composite structure, resulting in a rougher surface and subsequent increase of the functional groups (confirmed by FT-IR and XRD). These findings further validate the successful synthesis of the functionalized (FBKC) biochar-clay composite.

The obtained BET results demonstrated that the determined surface area (S_{BET}) of FBKC is 221.04 m²/g, which was approximately five-fold and thirty-fold higher than BC (47.02 m²/g) and KC (7.19 m²/g). Additionally, the total pore volume (TPV = 0.24 cm³/g) was significantly increased compared to the utilized precursors. The remarkable

increase in FBKC textural properties can be accredited to integrating KC and the impregnation of Fe-nanoparticles, which supplied more available sorption sites for removing NFX and CVD. These findings were corroborated by the FTIR and XRD results, which demonstrated an expansion in the KC interlayer space and the inclusion of new functional groups in FBKC.

3.2. Batch sorption studies

3.2.1. Effect of pH

The solution pH plays a crucial role in governing the sorption of antibiotics and dyes onto FBKC composites. The solution pH additionally affects the molecular state of the targeted pollutants and the surface charge of sorbents, which are dependent on the pH_{zpc} of the solid phases. The results of the stability investigation confirmed that FBKC composite is chemically stable in a strongly acidic medium and the measured pH_{zpc} value of FBKC was found to be 5.73 (see supplementary material), indicating that FBKC surface carries a positive charge at pH values below the pH_{zpc} and, conversely, a negative charge at pH values above the pH_{zpc} value. The obtained data showed that the sorbed amount of NFX was progressively increased as the solution pH increased (see supplementary material). The highest NFX sorption by FBKC was exhibited at pH 6, followed by a gradual decrease up to pH 9. This phenomenon can be explained due to the ionic speciation forms of NFX and pH_{zpc} of FBKC. The acid dissociation constants (pK_a) values of NFX are found to be 6.22 and 8.51 for the first and second dissociation constants (pK_{a1} and pK_{a2}), respectively (Jiang et al., 2023). The NFX molecules exhibit three distinct structural configurations depending on the solution pH level. In the acidic medium ($pH < pK_{a1}$ (=6.22)), the NFX cationic form (NFX^+) is the dominant form in the solution (carboxyl group). In the alkaline medium, when the solution pH is beyond pK_{a2} (=8.51), NFX is mainly anionic form (NFX^-) due to deprotonation of the amine group (at piperazine moiety). However, in the solution pH range between pK_{a1} (6.22) and pK_{a2} (8.51), zwitterionic form (NFX^\pm) is the dominant species due to the protonation and deprotonation processes of the amine groups and carboxylic acid, respectively (Chen et al., 2022). In fact NFX exhibited cationic form (NFX^+) in pH less than 6.22, and FBKC surface carries a positive charge at the same pH range. Consequently, the low sorption capacity of NFX at the acidic medium could result from electrostatic repulsion initiated by positively charged NFX and FBKC surfaces. The low sorption capacity of NFX at a pH levels above 7 could be ascribed to a similar mechanism as found at $pH < 7$. However, at pH range of 5.73 to 8.51, the NFX cationic and zwitterionic forms dominate, and the FBKC surface charge was negative, leading to electrostatic attraction.

Alternatively, the removal efficiency of CVD significantly increased from 74% (pH 2) to 100% (pH 8) (see supplementary material). The reduced sorption capacity observed in the acidic medium can be accredited to electrostatic repulsion between the positively charged surface of FBKC (resulting from the protonation of oxygen-containing functional groups) and the cationic species of CVD present in the solution. Indeed, considering the presence of two pK_a values for CVD (5.31 and 8.64) (Abdi et al., 2020), high sorption capacity exhibited by FBKC sorbent towards the CVD in an alkaline medium can be ascribed to the electrostatic attractive forces between the negatively charged deprotonated FBKC and the positively charged species of CVD. The findings demonstrated that an alkaline pH could enhance the elimination of CVD molecules. Nevertheless, FBKC demonstrated a high removal efficiency towards CVD, even in harsh acidic solutions. This suggests that the sorption of CVD onto the FBKC sorbent may be governed by other influential mechanisms such as H-bonding, pore-filling, and π - π stacking. Based on the experimental data for NFX and CVD, pH \approx 6 was selected as the optimum pH. Furthermore, the FBKC dosage was optimized (0.40 g/L). Fig. 2(a) illustrates the superior sorption performance of FBKC towards CVD compared to NFX, which demanded less FBKC dosage to reach the saturation plateau.

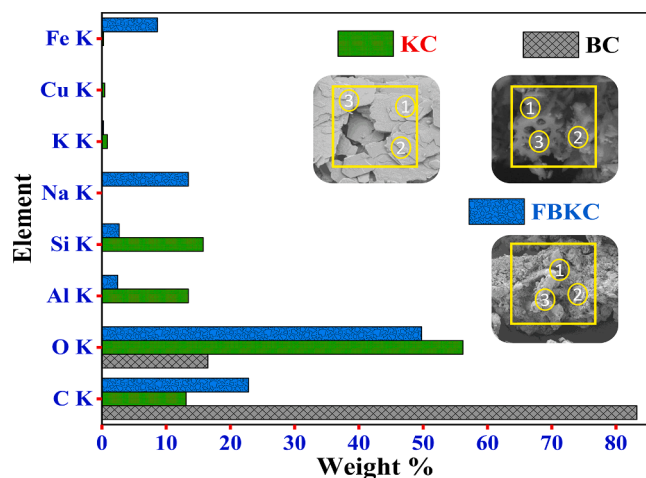


Fig. 1. EDS elemental analysis of BC, KC, and FBKC samples along with their corresponding SEM images.

3.2.2. Influence of ionic strength

Studying ionic strength is vital for comprehending and optimizing pollutant adsorption, as it reveals electrostatic interactions, solution chemistry, and treatment efficacy in complex environmental matrices. Assessing the sorption efficiency (%) index of FBKC sorbent towards CVD/NFX molecules in the presence of dissolved background ions (NaCl) (Fig. 2(b)), intended to simulate the components found in industrial wastewater, is adequate. A slight loss in the CVD removal (from 100.00 to 96.10%) by FBKC sorbent was recorded in the multi-component system (Fig. 2(b)). This can be ascribed to the effect of NaCl, which leads to the shielding of surface active sites by increasing the ionic strength of the aqueous media and varying the dye solubility (Ding et al., 2022). In the case of NFX, different sorption trend was observed (Fig. 2(b)), the NFX removal (%) slightly increased from 82.00 to 84.10% at the low electrolyte concentrations (up to 0.04 M), followed by a marginal decrease with increasing the electrolyte concentrations (up to 0.10 M). This observation can be ascribed to the salting-out phenomenon, which enhances the activity coefficient of hydrophobic organic compounds (Maged et al., 2021).

3.2.3. Reusability of the spent sorbent

The sorbent reusability is a vital aspect of the treatment processes, as it promotes economic viability, sustainability, waste reduction, and long-term effectiveness. Two distinct regeneration agents (NaOH and methanol) were utilized to regenerate the active sorption sites of the spent FBKC sorbent (Fig. 2(c)). Intriguingly, the removal efficiency of FBKC, in the case of NaOH eluent, showed only a slight decrease in the removal of CVD (from 100.00 to 92.46%) and NFX (from 83.00 to 80.19%) after the 5th cycle of sorption-desorption (Fig. 2(c)). The considerable maintained sorption efficiency after the 5th cycle can be accredited to the original character of FBKC. The phenomenon can also be credited to the protonation of the surface charge of FBKC by NaOH eluent. Moreover, the observed slight decrease can be attributed to the loss of a specific quantity of the utilized FBKC sorbent mass during the

regeneration process and/or the obstruction of active sorption sites (Elgarahy et al., 2023b). Contrarily, using methanol as eluent was found to be less efficient in the case of FBKC-CVD regeneration (decreased from 100.00 to 22.11%) (Fig. 2(c)). This can be ascribed to the less regeneration performance of methanol to reactivate the occupied binding sites by CVD of FBKC (Yan et al., 2023). However, the same eluent was relatively convincing in the case of NFX (Fig. 2(c)). The observed outcomes in the subsequent sorption-desorption experiments prioritized NaOH as a preferred eluent for the desorption of CVD and NFX, thus confirming the reliability of FBKC sorbent during multiple recycling phases.

3.2.4. Influence of contact time (kinetic modeling)

The sorption capacities of FBKC for CVD and NFX were assessed as a function over a time range of 360 min (Fig. 2(d)). The experimental data demonstrated a sharp increase in the sorption capacity of FBKC for CVD within the initial 30 min (quick initial sorption), reaching approximately 73.56% removal (Fig. 2(d)). However, the removal of NFX required about 100 min to get a similar removal percentage (Fig. 2(d)). The enhanced sorption rate monitored during the initial stages was facilitated via the concentration gradient existing between the unoccupied sorptive sites/functional groups of FBKC and the readily accessible CVD/NFX molecules (Mahmoud et al., 2021). Furthermore, as the contact time increased, the sorption rate progressively decreased until it reached a stagnant state (equilibrium), indicating that no further sorption occurred (reached a plateau) (Yao et al., 2021). Fig. 2(d) exhibits the fitting curves for three kinetic (pseudo-1st order, pseudo-2nd order, and Elovich) models along with the corresponding calculated parameter values (Table 1). The kinetic data of FBKC exhibited a good fit with the pseudo 2nd order model (R^2 of 0.99) for both CVD and NFX compared to the other employed models (Table 1). Following the experimental data to this model implies the presence of strong chemisorption interactions between FBKC and CVD/NFX molecules, such as ion exchange chemical reactions, complexation, pore filling, and H-bonding reactions (Liao

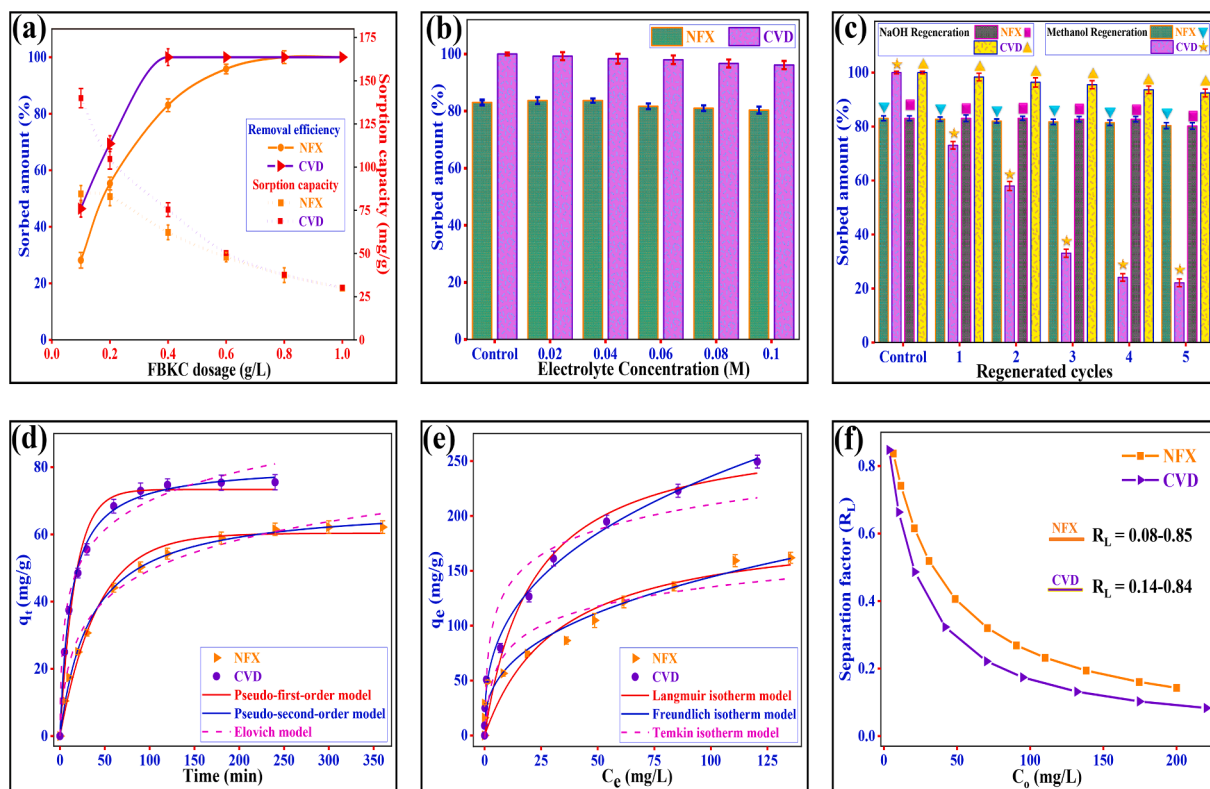


Fig. 2. (a) Effect of sorbent dosage, (b) Effect of ionic strength, (c) Regeneration studies (eluent: NaOH and methanol), (d) Non-linear sorption kinetic modeling, (e) Non-linear sorption isotherm modeling, and (f) Plot of separation factor (R_L) for NFX and CVD sorption onto FBKC.

et al., 2023). The theoretical sorption capacities ($q_{e,cal}$), as determined by pseudo 2nd order model, were found in agreement with the experimental value, confirming the validity of the best fitted model. Furthermore, the estimated initial sorption rate (v_0) for CVD dye was found to be three-fold higher than NFX (Table 1). This finding explains the faster initial sorption of CVD (30 min) compared to NFX (100 min) (Maged et al., 2023c).

3.2.5. Influence of initial concentration of pollutants (Isotherm modeling)

Generally, the sorption capacity of FBKC for CVD/NFX exhibited a gradual increase as the primary concentration was increased up to 300 mg/L (Fig. 2(e)). This can be attributed to the availability of an adequate number of accessible vacant sorptive sites within the porous structure of FBKC. This can also be attributed to the reduced steric repulsive forces between the adsorbed and diffused CVD/NFX molecules. At higher CVD/NFX concentrations, there was an associated increase in the frequency of effective collisions between CVD/NFX and FBKC composite (Fig. 2(e)). Consequently, more CVD/NFX molecules were captured within the binding sites of FBKC, driven by concentration gradient phenomenon (Aina et al., 2023; Hu et al., 2021). This led to an enhancement in the sorption capacity of FBKC sorbent. The experimental data obtained was further employed to assess the CVD/NFX sorption onto FBKC via fitting to three non-linearized isotherms (Freundlich, Temkin, and Langmuir) models (Fig. 2(e)), and their parameters were calculated (Table 1). The Freundlich isotherm model, based on R^2 and RMSE, provided the best fit for the isotherm data of FBKC towards CVD and NFX molecules. Hence, the sorption of CVD and

NFX occurred on heterogeneous surfaces of FBKC, indicating that it was a multilayer process. Moreover, these findings were consistent with the results obtained from kinetic modeling, suggesting that the adsorption process could involve multiple mechanisms. Consequently, the sorption of CVD and NFX by FBKC could occur via both physisorption and chemisorption (Maged et al., 2021). Furthermore, the maximum sorption (monolayer) capacity, via the Langmuir model, of NFX and CVD on FBKC composite was found to be 192.80 and 281.24 mg/g, respectively (Table 1). Furthermore, the favorability of the sorption process was assessed by determining R_L (dimensionless constant separation factor (Fig. 2(f))) values of FBKC for CVD/NFX molecules and was found in the range between 0 and 1 (Table 1). These findings suggest the favorability of sorption process and imply a strong binding between CVD/NFX molecules and FBKC (Saini et al., 2023).

3.3. The proposed sorption mechanisms

The physicochemical characterization, sorption data, and theoretical models were all combined to get insight into the possible confirmed mechanisms involved in the CVD/NFX sorption onto FBKC. Kaolinitic clay, utilized as a naturally occurring adsorbent, is acknowledged for its significant cation exchange capacity, particularly for cationic contaminants. On the other hand, biochar derived from algal biomass exhibits versatile capabilities to effectively eliminate various types of pollutants. Moreover, introducing Fe_xO_y nanoparticles, via the co-precipitation method, to the obtained composite resulted in a significant increase in physicochemical properties of BCKC (biochar-clay composite before

Table 1
The model (kinetic and isotherm) parameters of NFX and CVD sorption onto FBKC sorbent.

Pollutants	<i>Pseudo-first-order kinetic model</i> ($q_t = q_e(1 - e^{-k_1 t})$)				
	k_1 (1/min)	$q_{e,cal}$ (mg/g)	$q_{e,exp}$ (mg/g)	RMSE	R^2
NFX	0.02 ± 0.002	56.35 ± 1.26	63.17	6.76	0.986
CVD	0.05 ± 0.006	68.37 ± 1.77	75.53	14.33	0.978
	<i>Pseudo-second-order kinetic model</i> ($q_t = \frac{k_2 q_e^2 t}{1 + k_2 q_e t}$)				
	k_2 (g/mg min)	$q_{e,cal}$ (mg/g)	$q_{e,exp}$ (mg/g)	v_0 (mg/g min)	RMSE
NFX	$4.26 \times 10^{-4} \pm 2.39 \times 10^{-5}$	69.22 ± 0.81	63.17	2.04	1.14
CVD	$0.001 \pm 6.80 \times 10^{-5}$	80.88 ± 0.99	75.53	6.54	2.31
	<i>Elovich kinetic model</i> ($q_t = \left(\frac{1}{\beta}\right) \ln(1 + \alpha \beta t)$)				
	α (mg/g min)	β (g/min)	$q_{e,exp}$ (mg/g)	RMSE	R^2
NFX	5.19 ± 0.11	0.08 ± 0.005	63.17	4.00	0.975
CVD	32.76 ± 1.35	$0.079 \pm 7.2 \times 10^{-4}$	75.53	9.32	0.944
	<i>Langmuir isotherm model</i> ($q_e = \frac{q_m K_L C_e}{1 + K_L C_e}$)				
	$q_{max(cal)}$ (mg/g)	K_L (dm ³ /mg)	R_L	RMSE	R^2
NFX	192.80 ± 29.60	0.03 ± 0.01	0.14–0.84	36.77	0.877
CVD	281.24 ± 24.92	0.05 ± 0.01	0.08–0.85	32.47	0.961
	<i>Freundlich isotherm model</i> ($q_e = K_F C_e^{1/n}$)				R^2
	K_F (mg/g) (L/mg) ^{1/n}	n	RMSE		
NFX	26.55 ± 4.60	0.37 ± 0.04	10.36		0.950
CVD	45.56 ± 3.46	0.36 ± 0.02	5.37		0.993
	<i>Temkin isotherm model</i> ($q_e = \frac{RT}{b} \ln K_T C_e$)				R^2
	K_T (L/g)	b	RMSE		
NFX	2.04 ± 1.63	25.44 ± 4.64	38.51		0.873
CVD	5.81 ± 3.38	33.06 ± 4.05	63.53		0.924

modification), such as mesopore structure and specific surface area. This procedure was highly advantageous because it significantly increased the availability of sorption sites, thereby improving the removal efficiency of CVD and NFX.

Based on the FTIR spectra for FBKC, FBKC-CVD, CVD, FBKC-NFX, and NFX, the results showed that the $C=C$ vibration band between 1480 and 1635 cm^{-1} (FBKC) was shifted towards the lower wavelength and decreased its intensity after the sorption of NFX and CVD molecules. Additionally, the FTIR band of FBKC at 2945 cm^{-1} disappeared in FBKC-CVD and FBKC-NFX. These findings confirmed the contribution of the π - π electron donor-acceptor interactions between the electron-rich biochar (resulting from the presence of arene groups) and the electron-deficient of CVD/NFX molecules (Elgarahy et al., 2023a; Peiris et al., 2017). These findings further confirmed the superior sorption of FBKC for NFX in the zwitterionic form and CVD in the cationic form (confirmed via pH-edge experiments section; Section 3.2.1). The exchangeable cations present in KC may plausibly engage in interactions with the NFX (zwitterionic) and CVD (cationic) molecules (Li et al., 2018). Moreover, a notable decrease and disappearance of $O-H$ group ($\approx 3500 \text{ cm}^{-1}$) corresponds to KC, after sorption in addition to SiO_2 absorption bands were observed. These bands variation could be attributed to the surface, edges, and interlayer spaces of KC especially after the magnetic functionalization (Chen et al., 2016). Furthermore, the FTIR peak intensity of $C=O$ at 3490 cm^{-1} extensively decreased/disappeared after CVD/NFX sorption owing to the formation of hydrogen bonds with CVD and NFX molecules (Shi et al., 2023).

The stronger sorption of CVD/NFX molecules can be accredited to the electrostatic interactions between the varied functional groups of FBKC, which compete with the functional groups of CVD/NFX molecules (coulombic attraction with amide group) (Atugoda et al., 2021). This finding can explain the heterogeneity character deduced from the kinetic modeling of FBKC. However, the sorption mechanism of organic contaminants onto biochar involves two distinct types of interactions: sorption onto the carbonized fraction of BC and partitioning within the non-carbonized fractions of BC (Ashiq et al., 2019). The experimental

sorption results showed the superior performance of FBKC towards CVD compared to NFX. This superior sorption capacity can be attributed to the co-precipitation method using Fe(II) and Fe(III), which enhanced the existing cations on the FBKC surface. Consequently, the cation exchange capacity with CVD increased, owing to the natural cationic character of CVD. Besides, the capturing capacities of FBKC (Fe ions) combined with silicon-oxygen tetrahedrons of KC in the occurrence of a stable $[\text{Si-O}]$ and $[\text{HO-Fe}]$ via H bonding (confirmed via FTIR and XRD). The binding groups on FBKC (Fe-OH_2^+ and Fe-OH) demonstrated a strong affinity for CVD molecules by exchanging ($-\text{OH}^-$) groups on the sorbent's surface, resulting in the formation of mononuclear monodentate and binuclear bidentate inner-sphere complexes (Maged et al., 2023c). Moreover, the obtained Raman analysis demonstrated a noticeable decrease in the I_D/I_G ratio for FBKC after CVD and NFX sorption. This observed decrease revealed strong π - π stacking between FBKC, CVD, and NFX. It was noticed that the low I_D/I_G ratio for FBKC-CVD, compared to FBKC-NFX, indicated the high contribution of π - π stacking mechanism for CVD sorption compared to NFX sorption (Li et al., 2021). Furthermore, the SEM results for FBKC after CVD and NFX sorption revealed that the surface of FBKC exhibited a compact and smoother appearance, which can be attributed to pore blockage. This phenomenon confirms that the pore-filling effect mechanism and surface complexation were also involved in CVD and NFX sorption.

3.4. Dynamic sorption (continuous flow system)

3.4.1. Influence of operating parameters

Based on the optimum batch system conditions, the dynamic sorption (fixed-bed column) studies were conducted to assess the practical applicability (scale-up process) of FBKC towards CVD/NFX removal. Four experimental runs were performed for each pollutant (CVD and NFX), including inlet CVD/NFX concentration (feeding adsorbate of 15.00 and 25.00 mg/L), adsorbate flow rate (1.50 and 3.00 mL/min), and packed FBKC amount (bed height of $\approx 0.50 \text{ cm}$ (50 mg) and $\approx 1 \text{ cm}$ (100 mg)) in the column (breakthrough curves plots) (Fig. 3).

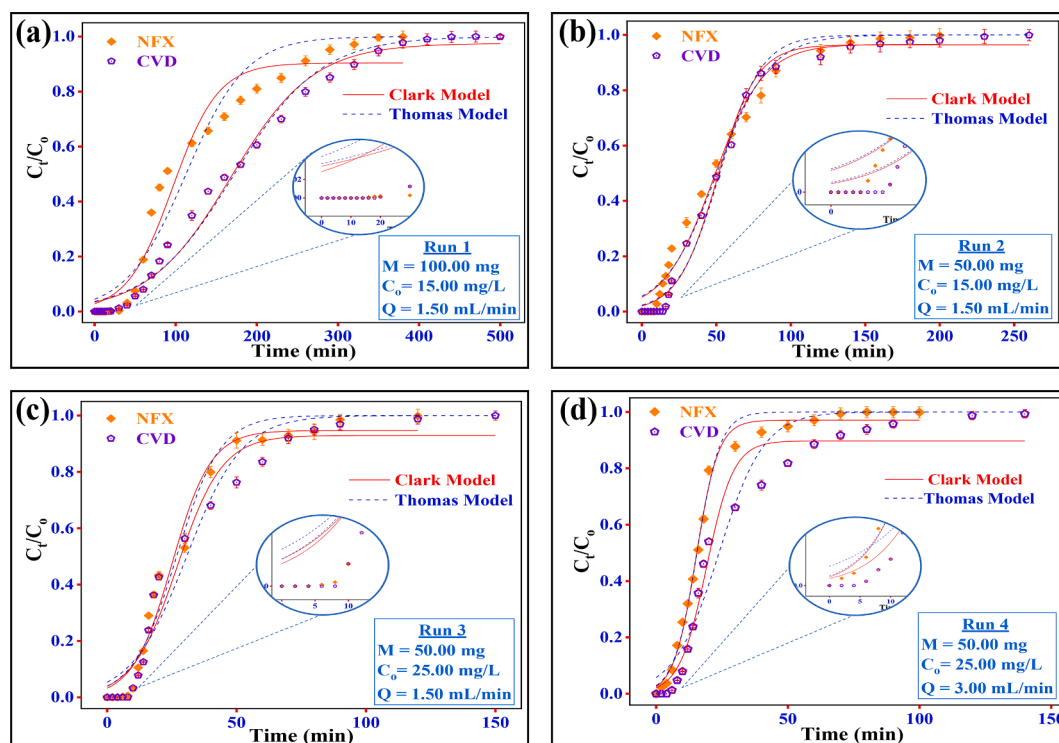


Fig. 3. Breakthrough curves of NFX and CVD sorption onto FBKC at (a) Run 1, (b) Run 2, (c) Run 3, and (d) Run 4, along with their corresponding applied kinetic models.

Table 2

The effect of flow rate, FBKC loading, and initial NFX/CVD concentration on the total adsorbed NFX/CVD (q_{total}), equilibrium uptake (q_{bed}), total removal efficiency of the column ($RE\%$) and total unadsorbed NFX/CVD concentration at equilibrium (C_{eq}) for FBKC sorbent.

Experiments Parameters	Run 1		Run 2		Run 3		Run 4	
	NFX	CVD	NFX	CVD	NFX	CVD	NFX	CVD
C_o (mg/L)	15.00		15.00		25.00		25.00	
Q (mL/min)	1.50		1.50		1.50		3.00	
M_{FBKC} (mg)	100		50		50		50	
V_{eff} (mL)	700	1000	400	520	180	225	300	420
t_b (min)	15	20	9	14	8	8	3	5
t_{total} (min)	380	500	200	260	120	150	100	140
q_{total} (mg)	3.79	5.39	1.63	1.76	1.15	1.31	1.69	2.32
q_{bed} (mg/g)	37.90	53.98	32.54	35.25	33.86	46.39	22.92	26.20
m_{total} (mg)	10.62	15.21	6.07	7.91	4.50	5.67	7.51	10.58
$RE(\%)$	35.70	35.48	26.83	22.28	25.44	23.11	22.56	21.92
C_{eq} (mg/L)	9.75	9.82	11.09	11.82	18.65	19.38	19.38	19.68

Furthermore, the obtained column parameters for FBKC were precisely calculated and tabulated in Table 2. The variation in bed height (FBKC loading amounts) within column experiments significantly influences fluid dynamics, mass transfer processes, and overall continuous flow system performance. The influence of packed FBKC amounts (Run 1–2) was plotted and presented in Fig. 3(a–b). The obtained breakthrough curve illustrated that increasing the packed bed height (from 0.50 to 1.00 cm) significantly improved the column performance, such as bed capacity (from 32.54 to 37.90 mg/g for NFX and from 35.25 to 53.98 mg/g for CVD). The impact of bed height on the column system was observed on breakthrough time and steepness (Fig. 3(a–b)), which showed approximately two-fold more with the higher bed height (1.00 cm (100 mg)) compared to the lower bed height for NFX and CVD pollutants (Table 2). The results revealed that increasing FBKC amounts within the columns (Run 1–2) leads to a proportional rise in the vertical extent of the bed inside the column. This finding can be ascribed to extending the physical interaction between CVD/NFX molecules and FBKC, sufficient available active sites, and intraparticle diffusion rate (Omitola et al., 2022).

Furthermore, the flow rate impact on CVD/NFX sorption was assessed by varying inlet flow rate (1.50 (Run 3) and 3.00 mL/min (Run 4)) with the remaining other parameters constant (50 mg; 25 mg/L) (Fig. 3(c–d)). Fig. 3(d) exhibited a decrease in breakthrough time (steeper curves) with an increase in flow rate, leading to steeper curves. However, the lower flow rate curves (1.50 mL/min (Run 3)) demonstrated a higher RE% and bed capacity compared to the higher flow rate (Table 2). These findings can be attributed to insufficient residence time, which hinders the interaction between FBKC and CVD/NFX molecules, ultimately reducing the binding potential between FBKC and CVD/NFX (Ahmed and Hameed, 2018). Furthermore, the feeding concentration influence on breakthrough curves for FBKC was evaluated using two different initial pollutant concentrations (15.00 mg/L (Run 2) and 25.00 mg/L (Run 3)) while other parameters were maintained. The primary observation for these two runs showed that the breakthrough time for FBKC was shortened with the higher inlet concentrations compared to the concentration of 15.00 mg/L for both NFX and CVD. The observed decrease in the breakthrough time could be accredited to the fast rate of occupying the accessible surface binding sites of FBKC (Dovi et al., 2022). Interestingly, increasing the inlet NFX and CVD concentration from 15.00 to 25.00 mg/L positively impacted the column parameters and performance. The calculated parameters showed increased bed capacity, especially for CVD (from 35.25 to 46.39 mg/g) (Table 2). This increase can be attributed to the heterogeneous character and multi-layer sorption of FBKC, which shows a higher sorption capacity with a higher concentration gradient.

3.4.2. Fixed-bed kinetic modeling

The obtained experimental breakthrough data (Run 1–4) were fitted (non-linear regression) to two fixed-bed kinetic models (Thomas and

Clark) (Fig. 3(a–b)). Thomas model was initially formulated based on the assumptions derived from the pseudo 2nd order kinetic and Langmuir isotherm models, which were initially developed for batch mode sorption systems. However, Clark model relies on two fundamental assumptions: (i) the inflow within the column behaves in a piston-like manner, and (ii) the mass transfer within the column follows the principles of the Freundlich isotherm model (Saini et al., 2023). The model's fitting (Fig. 3(a–b)) and calculated model's parameters confirmed that the experimental data greatly fitted to Thomas and Clark models. However, the Clark model's high R^2 values are within the range of 0.96 to 0.99, signifying its ability to effectively predict breakthrough curves for NFX and CVD (see supplementary material). The Clark model constant, denoted as r (indicates the mass transfer rate), revealed that a decline in mass transfer rate has occurred at higher concentrations, potentially attributed to active site saturation (Iheanacho et al., 2021). This outcome implies the considerable influence exerted by mass transfer and the heterogeneous nature of FBKC (Aryee and Han, 2022). The theoretical q_{TH} values derived from the Thomas model for all experimental runs closely aligned with the corresponding experimental q_{exp} values (Table 2). However, a negative correlation between K_{TH} values (the rate of solute transfer from the liquid phase to the solid phase (Dovi et al., 2021)) and increasing the inlet NFX/CVD concentrations was observed (see supplementary material). The observed results can be attributed to the enhanced driving force generated by the increasing concentrations of NFX/CVD, which facilitated mass transfer within the column (Maged et al., 2023c). These findings could also explain the established relationship between bed capacity and increasing the inlet NFX/CVD concentrations (mentioned in section 3.4.1.). Overall, the comparative analysis of the employed models indicated that the Clark model outperforms the other model in predicting the sorption behavior of NFX/CVD molecules onto FBKC in the continuous flow treatment system, indicating that NFX/CVD sorption occurred via a multi-layer process (Ostaszewski et al., 2022).

3.5. Cost estimation

Accurate cost estimation of biochar adsorbents is essential for evaluating their economic viability and potential for large-scale applications. The cost of biochar (composite) sorbents can vary depending on several factors, including feedstock cost, pyrolysis or carbonization process, and chemical activation or surface modification (if applied). It is crucial to consider the cost-effectiveness of biochar sorbents concerning their sorption capacity and ability to be reused. Higher-quality biochar sorbents with superior sorption performance may justify higher production costs due to their enhanced properties and longer lifespan, resulting in a more economical solution. The cost estimation for FBKC was determined using Eq. (1), which involves the breakdown of total costs into energy consumption ($\sum C_{energy}$; (€)) and feedstock/reagent expenses ($\sum C_{materials}$; (€)) (Chen et al., 2023).

Table 3

Cost analysis of producing 1 kg of FBKC composite.

Items	Consumed amount	Price (€)	Total cost (€)
Macro algae	1.00 kg	Free*	0.00
Kaolinitic Clay	1.00 kg	Free*	0.00
Tube furnace (874 W/h)	2.60 kW/h	0.05 €/kWh**	0.13
Atmospheric nitrogen (10 mL/min)	1.80 L	0.38 €/L	0.68
Chemicals	76.00 g	0.06 €/g	4.56
Drying oven (425 W/h)	5.10 KW/h	0.05 €/kWh**	0.26
Total			5.72

* Collected by the authors without cost.

** The price (0.05 €/kWh) is according to halvinsäkösimus.fi /2023.

$$Total\ cost = \sum C_{energy} + \sum C_{materials} \quad (1)$$

The detailed preparation costs of FBKC were analyzed (Table 3). The preparation cost of FBKC was calculated to be 5.72 €/kg, which is a relatively low-cost sorbent targeting these kinds of pollutants compared to activated carbon, ion-exchange resins, and membranes. The low synthesis cost of FBKC can be ascribed to the negligible feedstock costs (zero cost), reduced electricity consumption, and low-cost modification methods (Table 3). One of the advantages of FBKC is the magnetic character of the obtained sorbent, saving the filtration costs. Notably, the cost can be further decreased when the process is applied on the industrial scale for producing a higher amount of FBKC. Additionally, treating the actual wastewater (less pollutant concentrations) will consume less amount of the obtained sorbent, as FBKC has a high sorption capacity. Therefore, the cost estimation analysis provides conclusive evidence of the substantial capacity of FBKC to address various pollutants, such as pharmaceutical compounds and dyes, at a reasonable cost.

4. Conclusions

The engineered FBKC, derived from algal biochar and kaolinitic clay, and functionalized via the co-precipitation method exhibited superior NFX/CVD sorption compared to original precursors due to the improved active sites offered from BC, KC, and Fe nanoparticles. FBKC showed enhanced S_{BET} (221.04 m²/g) and maximum bed capacity of 37.90 and 53.98 mg/g for NFX and CVD in continuous flow mode, respectively. The fitted theoretical models suggested the corporative heterogeneous sorption process. The obtained characterization results confirmed the abundance of FBKC functional groups contributed to the sorption process. The study provides environmentally sustainable biochar composite sorbent for emergent contaminants mitigation at a reasonable cost.

Declaration of Competing Interest

The authors declare that they have no known competing financial interests or personal relationships that could have appeared to influence the work reported in this paper.

Data availability

Data will be made available on request.

Acknowledgments

The authors are thankful to Liisa Puro and Timo Laakso for their kind assistance in some characterization analyses. The authors (A.M., M.W. H., and N.H.H.) are grateful for the partial financial support toward this study by the Federal Ministry of Education, Science, and Research (BMBWF) through Austria's Agency for Education and

Internationalization (OeAD) [Grant Number: Africa UNINET P056]. The authors would also like to thank the Editor and the anonymous reviewers for providing their insightful comments and suggestions to improve the quality of this work.

Appendix A. Supplementary data

Supplementary data to this article can be found online at <https://doi.org/10.1016/j.biortech.2023.129593>.

References

- Abd El-Fattah, H., Maged, A., Kamel, R., Kharbush, S., 2023. Recent technologies for the elimination of pharmaceutical compounds from aqueous solutions: A review. *Front. Sci. Res. Technol.* 5 (1) <https://doi.org/10.21608/FSRT.2023.173676.1074>.
- Abdi, M., Balagabri, M., Karimi, H., Hossini, H., Rastegar, S.O., 2020. Degradation of crystal violet (CV) from aqueous solutions using ozone, peroxone, electroperoxone, and electrolysis processes: a comparison study. *Appl. Water Sci.* 10, 1–10. <https://doi.org/10.1007/s13201-020-01252-w>.
- Ahmed, M.J., Hameed, B.H., 2018. Removal of emerging pharmaceutical contaminants by adsorption in a fixed-bed column: A review. *Ecotoxicol. Environ. Saf.* 149, 257–266. <https://doi.org/10.1016/j.ecoenv.2017.12.012>.
- Aina, S.T., Kyomuhimbo, H.D., Ramjee, S., Du Plessis, B., Mjimba, V., Maged, A., Haneklaus, N., Brink, H.G., 2023. Synthesis and Assessment of Antimicrobial Composites of Ag Nanoparticles or AgNO₃ and Egg Shell Membranes. *Molecules* 28, 4654. <https://doi.org/10.3390/molecules28124654>.
- Al-Lagtah, N.M.A., Al-Muhtaseb, A.H., Ahmad, M.N.M., Salameh, Y., 2016. Chemical and physical characteristics of optimal synthesised activated carbons from grass-derived sulfonated lignin versus commercial activated carbons. *Microporous Mesoporous Mater.* 225, 504–514. <https://doi.org/10.1016/j.micromeso.2016.01.043>.
- Aneesh, E.M., Anoopkumar, A.N., Madhavan, A., Sindhu, R., Binod, P., Kuddus, M., Ruiz, H.A., Pandey, A., Awasthi, M.K., Show, P.L., 2023. Inferences on bioengineering perspectives and circular economy to tackle the emerging pollutants. *Environ. Technol. Innov.* 30, 103116. <https://doi.org/10.1016/j.eti.2023.103116>.
- Aryee, A.A., Han, R., 2022. A novel biocomposite based on peanut husk with antibacterial properties for the efficient sequestration of trimethoprim in solution: Batch and column adsorption studies. *Colloids Surfaces A Physicochem. Eng. Asp.* 635, 128051. <https://doi.org/10.1016/j.colsurfa.2021.128051>.
- Ashiq, A., Adassooriya, N.M., Sarkar, B., Rajapaksha, A.U., Ok, Y.S., Vithanage, M., 2019. Municipal solid waste biochar-bentonite composite for the removal of antibiotic ciprofloxacin from aqueous media. *J. Environ. Manage.* 236, 428–435. <https://doi.org/10.1016/j.jenvman.2019.02.006>.
- Atugoda, T., Gunawardane, C., Ahmad, M., Vithanage, M., 2021. Mechanistic interaction of ciprofloxacin on zeolite modified seaweed (Sargassum crassifolium) derived biochar: Kinetics, isotherm and thermodynamics. *Chemosphere* 281, 130676. <https://doi.org/10.1016/j.chemosphere.2021.130676>.
- Chen, L., Zhou, C.H., Fiore, S., Tong, D.S., Zhang, H., Li, C.S., Ji, S.F., Yu, W.H., 2016. Functional magnetic nanoparticle/clay mineral nanocomposites: Preparation, magnetism and versatile applications. *Appl. Clay Sci.* 127, 143–163. <https://doi.org/10.1016/j.clay.2016.04.009>.
- Chen, L., Mi, B., He, J., Li, Y., Zhou, Z., Wu, F., 2023. Functionalized biochars with highly-efficient malachite green adsorption property produced from banana peels via microwave-assisted pyrolysis. *Bioresour. Technol.* 376, 128840. <https://doi.org/10.1016/j.biortech.2023.128840>.
- Chen, J., Tan, L., Cui, Z., Qu, K., Wang, J., 2022. Graphene Oxide Molecularly Imprinted Polymers as Novel Adsorbents for Solid-Phase Microextraction for Selective Determination of Norfloxacin in the Marine Environment. *Polymers (Basel)* 14, 1839. <https://doi.org/10.3390/polym14091839>.
- Ding, H., Zhang, Z., Li, Y., Ding, L., Sun, D., Dong, Z., 2022. Fabrication of novel Fe/Mn/N co-doped biochar and its enhanced adsorption for bisphenol A based on π - π electron donor-acceptor interaction. *Bioresour. Technol.* 364, 128018. <https://doi.org/10.1016/j.biortech.2022.128018>.

- Dovi, E., Aryee, A.A., Kani, A.N., Mpatani, F.M., Li, J., Qu, L., Han, R., 2021. Functionalization of walnut shell by grafting amine groups to enhance the adsorption of Congo red from water in batch and fixed-bed column modes. *J. Environ. Chem. Eng.* 9 (5), 106301. <https://doi.org/10.1016/j.jece.2021.106301>.
- Dovi, E., Aryee, A.A., Kani, A.N., Mpatani, F.M., Li, J., Qu, L., Han, R., 2022. High-capacity amino-functionalized walnut shell for efficient removal of toxic hexavalent chromium ions in batch and column mode. *J. Environ. Chem. Eng.* 10 (2), 107292. <https://doi.org/10.1016/j.jece.2022.107292>.
- Elgarahy, A.M., Maged, A., Elloff, M.G., Zahran, M., Kharbush, S., Elwakeel, K.Z., Bhatnagar, A., 2023a. Geopolymers as sustainable eco-friendly materials: Classification, synthesis routes, and applications in wastewater treatment. *Sep. Purif. Technol.* 324, 124631. <https://doi.org/10.1016/j.seppur.2023.124631>.
- Elgarahy, A.M., Maged, A., Elwakeel, K.Z., El-Gohary, F., El-Qelish, M., 2023b. Tuning cationic/anionic dyes removal from aqueous solution onto green algal biomass for biohydrogen production. *Environ. Res.* 216, 114522 <https://doi.org/10.1016/j.envres.2022.114522>.
- Foong, S.Y., Chan, Y.H., Chin, B.L.F., Lock, S.S.M., Yee, C.Y., Yiin, C.L., Peng, W., Lam, S. S., 2022. Production of biochar from rice straw and its application for wastewater remediation – An overview. *Bioresour. Technol.* <https://doi.org/10.1016/j.biortech.2022.127588>.
- Hu, M., Deng, W., Hu, M., Chen, G., Zhou, P., Zhou, Y., Su, Y., 2021. Preparation of binder-less activated char briquettes from pyrolysis of sewage sludge for liquid-phase adsorption of methylene blue. *J. Environ. Manage.* 299, 113601 <https://doi.org/10.1016/j.jenvman.2021.113601>.
- Iheanacho, O.C., Nwabanne, J.T., Obi, C.C., Onu, C.E., 2021. Packed bed column adsorption of phenol onto corn cob activated carbon: linear and nonlinear kinetics modeling. *South African J. Chem. Eng.* 36, 80–93. <https://doi.org/10.1016/j.sajce.2021.02.003>.
- Jiang, X., An, Y., Huang, Y., Ding, W., Sun, M., Li, H., Zheng, H., 2023. One pot synthesis of Cu–Ni–S@Ni foam for the simultaneous removal and detection of norfloxacin. *J. Clean. Prod.* 382, 135385 <https://doi.org/10.1016/j.jclepro.2022.135385>.
- Li, Y., Zeng, C., Wang, C., Zhang, L., 2018. Preparation of C@silica core/shell nanoparticles from ZIF-8 for efficient ciprofloxacin adsorption. *Chem. Eng. J.* 343, 645–653. <https://doi.org/10.1016/j.cej.2018.01.147>.
- Li, B., Zhang, Y., Xu, J., Xie, Z., Tang, J., Li, X., Fan, S., 2021. Simultaneous carbonization, activation, and magnetization for producing tea waste biochar and its application in tetracycline removal from the aquatic environment. *J. Environ. Chem. Eng.* 9 (4), 105324. <https://doi.org/10.1016/j.jece.2021.105324>.
- Liao, X., Chen, C., Liang, Z., Zhao, Z., Cui, F., 2023. Selective adsorption of antibiotics on manganese oxide-loaded biochar and mechanism based on quantitative structure–property relationship model. *Bioresour. Technol.* 367, 128262 <https://doi.org/10.1016/j.biortech.2022.128262>.
- Maged, A., Ismael, I.S., Kharbush, S., Sarkar, B., Peräniemi, S., Bhatnagar, A., 2020. Enhanced interlayer trapping of Pb(II) ions within kaolinite layers: intercalation, characterization, and sorption studies. *Environ. Sci. Pollut. Res.* 27, 1870–1887. <https://doi.org/10.1007/s11356-019-06845-w>.
- Maged, A., Dissanayake, P.D., Yang, X., Pathirannahalage, C., Bhatnagar, A., Ok, Y.S., 2021. New mechanistic insight into rapid adsorption of pharmaceuticals from water utilizing activated biochar. *Environ. Res.* 202, 111693 <https://doi.org/10.1016/j.envres.2021.111693>.
- Maged, A., Abu El-Magd, S.A., Radwan, A.E., Kharbush, S., Zamzam, S., 2023a. Evaluation insight into Abu Zenima clay deposits as a prospective raw material source for ceramics industry: Remote Sensing and Characterization. *Sci. Rep.* 13, 1–16. <https://doi.org/10.1038/s41598-022-26484-5>.
- Maged, A., El-Fattah, H.A., Kamel, R.M., Kharbush, S., Elgarahy, A.M., 2023b. A comprehensive review on sustainable clay-based geopolymers for wastewater treatment: circular economy and future outlook. *Environ. Monit. Assess.* 195, 693. <https://doi.org/10.1007/s10661-023-11303-9>.
- Maged, A., Elgarahy, A.M., Haneklaus, N.H., Gupta, A.K., Show, P.-L., Bhatnagar, A., 2023c. Sustainable functionalized smectitic clay-based nano hydrated zirconium oxides for enhanced levofloxacin sorption from aqueous medium. *J. Hazard. Mater.* 452, 131325 <https://doi.org/10.1016/j.jhazmat.2023.131325>.
- Mahmoud, M.E., Mohamed, A.K., Salam, M.A., 2021. Self-decoration of N-doped graphene oxide 3-D hydrogel onto magnetic shrimp shell biochar for enhanced removal of hexavalent chromium. *J. Hazard. Mater.* 408, 124951 <https://doi.org/10.1016/j.jhazmat.2020.124951>.
- Nguyen, T.B., Truong, Q.M., Chen, C.W., Chen, W.H., Dong, C.D., 2022. Pyrolysis of marine algae for biochar production for adsorption of Ciprofloxacin from aqueous solutions. *Bioresour. Technol.* 351, 127043 <https://doi.org/10.1016/j.biortech.2022.127043>.
- Ohale, P.E., Igwegbe, C.A., Iwuozor, K.O., Emenike, E.C., Obi, C.C., Białowiec, A., 2023. A review of the adsorption method for norfloxacin reduction from aqueous media. *MethodsX* 10, 102180. <https://doi.org/10.1016/j.mex.2023.102180>.
- Omitola, O.B., Abonyi, M.N., Akpomie, K.G., Dawodu, F.A., 2022. Adams-Bohart, Yoon-Nelson, and Thomas modeling of the fix-bed continuous column adsorption of amoxicillin onto silver nanoparticle-maize leaf composite. *Appl. Water Sci.* 12, 1–9. <https://doi.org/10.1007/s13201-022-01624-4>.
- Ostaszewski, P., Dugosz, O., Banach, M., 2022. Analysis of measuring methods of the concentration of methylene blue in the sorption process in fixed-bed column. *Int. J. Environ. Sci. Technol.* 19, 1–8. <https://doi.org/10.1007/s13762-021-03156-x>.
- Pandey, A., Govindwar, S., Kurade, M., Jeon, B., 2023. *Current Developments in Bioengineering and Biotechnology: Advances in Eco-friendly and Sustainable Technologies for the Treatment of Textile Wastewater*. Elsevier.
- Peiris, C., Gunatilake, S.R., Mlsna, T.E., Mohan, D., Vithanage, M., 2017. Biochar based removal of antibiotic sulfonamides and tetracyclines in aquatic environments: A critical review. *Bioresour. Technol.* 246, 150–159. <https://doi.org/10.1016/j.biortech.2017.07.150>.
- Qin, J., Ji, R., Sun, Q., Li, W., Cheng, H., Han, J., Jiang, X., Song, Y., Xue, J., 2023. Self-activation of potassium/iron citrate-assisted production of porous carbon/porous biochar composites from macroalgae for high-performance sorption of sulfamethoxazole. *Bioresour. Technol.* 369, 128361 <https://doi.org/10.1016/j.biortech.2022.128361>.
- Saini, K., Sahoo, A., Kumar, J., Kumari, A., Pant, K.K., Bhatnagar, A., Bhaskar, T., 2023. Effective utilization of discarded reverse osmosis post-carbon for adsorption of dyes from wastewater. *Environ. Res.* 231, 116165 <https://doi.org/10.1016/j.envres.2023.116165>.
- Sajjadi, B., Shrestha, R.M., Chen, W.Y., Mattern, D.L., Hammer, N., Raman, V., Dorris, A., 2021. Double-layer magnetized/functionalized biochar composite: Role of microporous structure for heavy metal removals. *J. Water Process Eng.* 39, 101677 <https://doi.org/10.1016/j.jwpe.2020.101677>.
- Shi, Q., Wang, W., Zhang, H., Bai, H., Liu, K., Zhang, J., Li, Z., Zhu, W., 2023. Porous biochar derived from walnut shell as an efficient adsorbent for tetracycline removal. *Bioresour. Technol.* 383, 129213 <https://doi.org/10.1016/j.biortech.2023.129213>.
- Uddin, M.K., Abd Malek, N.N., Jawad, A.H., Sabar, S., 2023. Pyrolysis of rubber seed pericarp biomass treated with sulfuric acid for the adsorption of crystal violet and methylene green dyes: an optimized process. *Int. J. Phytorem.* 25, 393–402. <https://doi.org/10.1080/15226514.2022.2086214>.
- Wang, Z., Yang, X., Qin, T., Liang, G., Li, Y., Xie, X., 2019. Efficient removal of oxytetracycline from aqueous solution by a novel magnetic clay–biochar composite using natural attapulgite and cauliflower leaves. *Environ. Sci. Pollut. Res.* 26, 7463–7475. <https://doi.org/10.1007/s11356-019-04172-8>.
- Yan, N., Hu, B., Zheng, Z., Lu, H., Chen, J., Zhang, X., Jiang, X., Wu, Y., Doling, J., Xu, L., 2023. Twice-milled magnetic biochar: A recyclable material for efficient removal of methylene blue from wastewater. *Bioresour. Technol.* 372, 128663 <https://doi.org/10.1016/j.biortech.2023.128663>.
- Yao, B., Luo, Z., Du, S., Yang, J., Zhi, D., Zhou, Y., 2021. Sustainable biochar/MgFe2O4 adsorbent for levofloxacin removal: Adsorption performances and mechanisms. *Bioresour. Technol.* 340, 125698 <https://doi.org/10.1016/j.biortech.2021.125698>.